

Variety of Planar Fourth-Order Fiber Orientation Tensors and Implications on Effective Elastic Stiffnesses

Julian Karl Bauer¹, Thomas Seelig², Andrew Hrymak³, and Thomas Böhlke^{1,*}

¹ Chair for Continuum Mechanics, Institute of Engineering Mechanics, Karlsruhe Institute of Technology (KIT), Germany

² Institute of Mechanics, Karlsruhe Institute of Technology (KIT), Germany

³ Department of Chemical and Biochemical Engineering, University of Western Ontario (UWO), Canada

In this contribution, selected results from [1–3] are presented in a compact and simplified way. In addition, the variety of fiber orientation tensors is used to determine a maximum deviation of the direction-dependent Young's modulus, which can arise if only second-order directional information is included in a specific meanfield homogenization. Focusing on the special case of planar fiber distributions, the variety of fiber orientation tensors identified in [1] is considered as a design space. This design space is completely explored for the orientation-averaging homogenization following [4], fixed material parameters and fixed fiber volume content. The possible directional dependence of the resulting effective stiffnesses is graphically presented using polar plots of the direction-dependent Young's modulus. These polar plots are arranged on two-dimensional slices within the parameter space of planar fourth-order fiber orientation tensors. This gives a complete representation of the influence of the orientation tensor on the anisotropic stiffness tensor. Consequences of closure approximations, i.e., restriction to second-order directional information, are demonstrated and motivate measurement of fourth-order fiber orientation tensors.

© 2023 The Authors. *Proceedings in Applied Mathematics & Mechanics* published by Wiley-VCH GmbH.

1 Introduction and Motivation

The mechanical properties of discontinuous fiber-reinforced composites [5] highly depend on the microstructure, including the amount and arrangement of the fibers. Information about the amount of fibers usually enters homogenization methods via the fiber volume fraction. Quantification of the arrangement of fibers can be challenging. The fiber orientation distribution function $\psi(\mathbf{n})$ quantifies the orientation of fibers in a given reference volume in terms of a one-point correlation function. This distribution is an exact measure for the orientation of fibers, but being a one-point correlation function it, e.g., lacks any information on the spatial arrangements of the fibers. For application in the three-dimensional real world, the orientation distribution function $\psi : \mathcal{S}^2 \rightarrow \mathbb{R}$ maps any direction, i.e., any point on the surface of the unit sphere \mathcal{S}^2 to a real number and specifies the relative volume fraction dv/v of fibers in direction \mathbf{n} , i.e.,

$$\frac{dv}{v}(\mathbf{n}) = \psi(\mathbf{n}) dS. \quad (1)$$

Integrating Equation 1 over a directional surface element, e.g., visualized in Figure 1, yields the relative volume fraction of fibers pointing into directions contained in this surface element. For practical applications, the distribution function is usually not available. An exception is given by direct fiber simulations [6], i.e., mold filling simulations, which directly resolve individual fibers or fiber groups instead of describing them on average using fiber orientation tensors. However, direct fiber simulations are computationally expensive and averages of the distribution in terms of fiber orientation tensors of order k

$$\mathbb{N}_{\langle k \rangle} = \int_{\mathcal{S}^2} \psi(\mathbf{n}) \mathbf{n}^{\otimes k} d\mathbf{n} \quad (2)$$

are an established averaged measure for the direction of fibers inside a local reference volume and can be directly obtained by flow simulations or computer tomography scans. Tensor orders two and four are commonly used

$$\mathbf{N} = \mathbb{N}_{\langle 2 \rangle} = \int_{\mathcal{S}^2} \psi(\mathbf{n}) \mathbf{n} \otimes \mathbf{n} d\mathbf{n}, \quad \mathbb{N} = \mathbb{N}_{\langle 4 \rangle} = \int_{\mathcal{S}^2} \psi(\mathbf{n}) \mathbf{n} \otimes \mathbf{n} \otimes \mathbf{n} \otimes \mathbf{n} d\mathbf{n}. \quad (3)$$

Several homogenization methods take the fiber orientation into account either directly in the case of, e.g., orientation-averaging meanfield homogenization [4, 7, 8] or indirectly via artificially generated microstructures [9–12] utilized in full-field homogenization [13, 14].

This work is motivated by the analysis of sheet molding compound (SMC), a discontinuous fiber-reinforced composite with fibers being significantly longer than the typical thickness of manufactured specimen. A microstructure of SMC, identified by computer tomography scans in [15], is repeated in Figure 2. This microstructure is influenced by the two-step manufacturing process of SMC depicted in Figure 6 and Figure 7. Although several fibers in Figure 2 are bent, we assume fibers in SMC to be straight. This assumption has also been made by [10] generating artificial SMC microstructures of which one is repeated in Figure 3. In consequence, the orientation of the fibers can be described by fiber orientation tensors.

* Corresponding author: e-mail thomas.boehlke@kit.edu, phone +49 721 608 48852



This is an open access article under the terms of the Creative Commons Attribution License, which permits use, distribution and reproduction in any medium, provided the original work is properly cited.

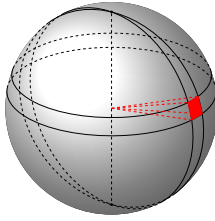


Fig. 1: Sphere surface in 3D and surface element

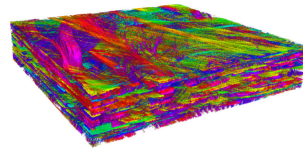


Fig. 2: Measured microstructure of sheet molding compound (SMC) [15]

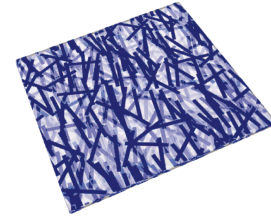


Fig. 3: Artificial microstructure of SMC [10]

2 Design space fiber orientation tensors

Fiber orientation tensors are usually seen as a directional measure representing averaged information of a given microstructure following Figure 4. From a simulation point of view, fiber orientation tensors also represent a design space for orientation-averaging homogenization methods. The space of admissible fiber orientation tensors \mathcal{N} , schematically depicted in Figure 5, can be represented by parameterizations of fiber orientation tensors combined with admissible parameter ranges. For several subspaces, motivated by material symmetry, admissible parameter ranges are identified in [1].



Fig. 4: Fiber orientation tensors as directional measure

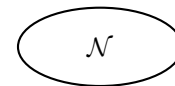


Fig. 5: Fiber orientation tensors as design space, Schematic representation of an admissible parameter space

The design space given by second-order fiber orientation tensors is known in literature [17–19]. Based on the eigensystem-based parameterization

$$\mathbf{N} = \int_{S^2} \psi(\mathbf{n}) \mathbf{n} \otimes \mathbf{n} \, d\mathbf{n} = \begin{bmatrix} \lambda_1 & 0 & 0 \\ & \lambda_2 & 0 \\ \text{sym} & & \lambda_3 \end{bmatrix} \mathbf{v}_i \otimes \mathbf{v}_j \quad \text{with } \mathbf{Q} = \mathbf{v}_i \otimes \mathbf{e}_i \in SO(3), \quad (4)$$

the space of admissible second-order fiber orientation tensors is given by

$$\mathcal{N}^{\mathbf{N}} = \left\{ \mathbf{N}(\lambda_1, \lambda_2) \mid \frac{1}{3} \leq \lambda_1 \leq 1, \frac{1}{2}(1 - \lambda_1) \leq \lambda_2 \leq \min(\lambda_1, 1 - \lambda_1) \right\} \quad (5)$$

and visualized in Figure 8. This visualization is known as the orientation triangle [19]. The variety of generic fourth-order fiber orientation tensors has not yet been expressed in closed form. However, following [1] a generic parameterization is given by

$$\mathbb{N}(\mathbf{N}, d_1, \dots, d_9) = \mathbb{N}^{\text{iso}} + \frac{6}{7} \text{sym}(\text{dev}(\mathbf{N}) \otimes \mathbf{I}) + \mathbb{F}^{\text{tricl}}(d_1, \dots, d_9) \quad (6)$$

with an irreducible structure tensor

$$\mathbb{F}^{\text{tricl}}(d_1, \dots, d_9) = \left[\begin{array}{ccc|ccc} -(d_1 + d_2) & d_1 & d_2 & -\sqrt{2}(d_4 + d_5) & \sqrt{2}d_6 & \sqrt{2}d_8 \\ & -(d_1 + d_3) & d_3 & \sqrt{2}d_4 & -\sqrt{2}(d_6 + d_7) & \sqrt{2}d_9 \\ & & -(d_2 + d_3) & \sqrt{2}d_5 & \sqrt{2}d_7 & -\sqrt{2}(d_8 + d_9) \end{array} \right] \mathbf{B}_\xi^v \otimes \mathbf{B}_\zeta^v \quad (7)$$

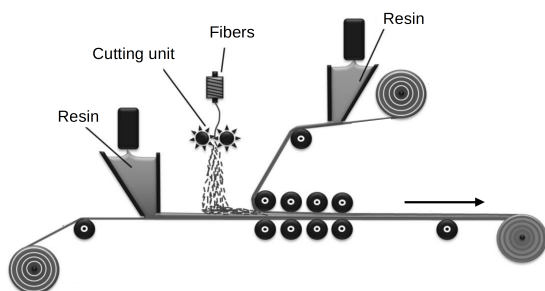


Fig. 6: Manufacturing process of semi-finished SMC adapted from [16]

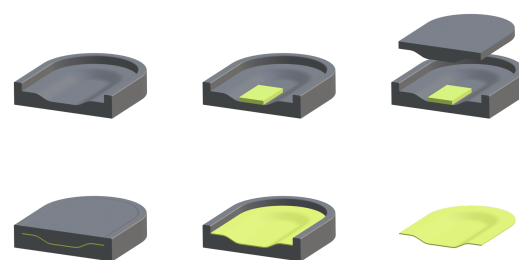


Fig. 7: Schematic compression molding process step of SMC, sequence evolving from left to right and top to bottom

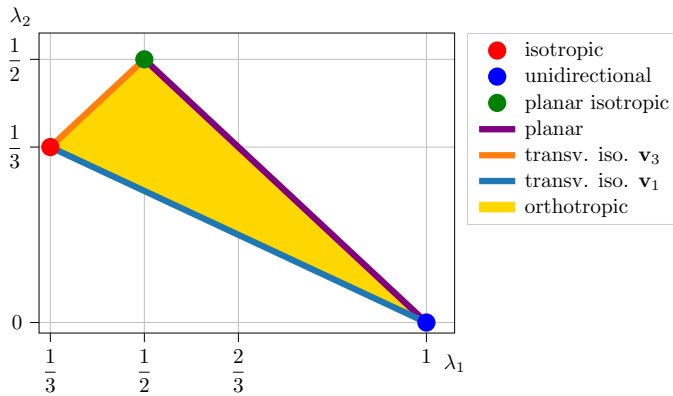


Fig. 8: Fiber orientation triangle representing the variety of second-order fiber orientation tensors following [1, Figure 1b] including material symmetries and other subspaces

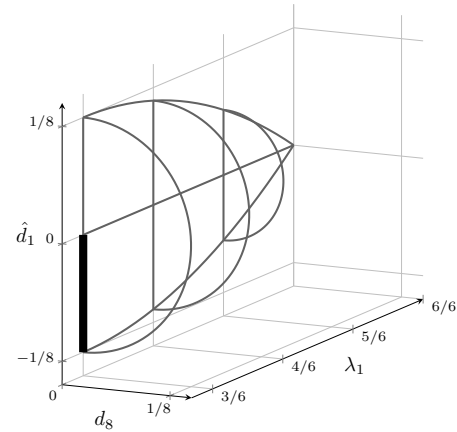


Fig. 9: Space of admissible and distinct planar fourth-order fiber orientation tensors following [3, Figure 2]. The bold bar in the plane $\lambda_1 = 1/2$ highlights the degeneration of this plane to a line, see [2, Section 2.2] for details.

given in Kelvin-Mandel notation [1, 20–22].

3 Planar subspace

The subspace of planar fiber distributions and corresponding fiber orientation tensors is relevant, e.g., for microstructures of plate-like long-fiber reinforced composites such as SMC. Planar second-order fiber orientation tensors are located on the upper right edge of the orientation triangle in Figure 8. Based on the parameterization $\mathbb{N}^{\text{planar}}(\lambda_1, d_1, d_8)$ in [2, Equation (15)], the parameterization

$$\mathbb{N}^{\text{planar}}(\lambda_1, \hat{d}_1, d_8) = \left[\begin{array}{cc|ccc} -\hat{d}_1 - \hat{R}(\lambda_1) + \lambda_1 & \hat{d}_1 + \hat{R}(\lambda_1) & 0 & 0 & 0 & \sqrt{2} d_8 \\ & -\hat{d}_1 - \hat{R}(\lambda_1) + (1 - \lambda_1) & 0 & 0 & 0 & -\sqrt{2} d_8 \\ \hline & & 0 & 0 & 0 & 0 \\ \text{completely} & & & & & \text{symmetric} \end{array} \right] \mathbf{B}_\xi^v \otimes \mathbf{B}_\zeta^v \quad (8)$$

with $\hat{R}(\lambda_1) = (\lambda_1 - \lambda_1^2)/2$ and $\hat{d}_1 = d_1 - \hat{R}(\lambda_1) + 4/35$ following [3], combined with the algebraic requirement of positive semi-definiteness of $\mathbb{N}^{\text{planar}}$ in the Kelvin-Mandel space, leads to the body of admissible and structurally distinct planar fourth-order fiber orientation tensors visualized as the wire-frame body in Figure 9. Algebraic expression for this body are given in [3, Equations (11) and (12)]. Two tensors are structurally distinct, if they differ by more than just a rotation, see also [2, Equation (18)].

4 Orientation-Averaging Meanfield Homogenization

Knowing the variety of fiber orientation tensors offers the possibility to draw a complete picture of the dependence of effective mechanical properties obtained by a given homogenization method, on varying microstructure. For several established meanfield homogenization methods the effective mechanical stiffness $\bar{\mathbb{C}}$ depends on fiber orientation tensors up to fourth-order, the mechanical properties of the single phases, e.g., matrix \mathbb{C}_m and fibers \mathbb{C}_f , as well as the volume fractions, e.g., fiber volume fraction v_f . This dependence is schematically depicted in Figure 10. In the following solely one specific meanfield homogenization method, Mori-Tanaka orientation averaging following Benveniste [4] is used. This homogenization method is selected due to its popularity. Details on this method can be found in [3, 4] and an open-source implementation in [23]. The fiber volume content and material properties of fiber and matrix are fixed to SMC-specific values given in [3, Table 1], originating from [8, Table 2].

5 Directional Variety of Effective Stiffnesses

Each point in the body of admissible planar fourth-order fiber orientation tensors in Figure 9 with vanishing value parameter d_8 represents an orthotropic fiber orientation tensor. In Figure 12, ten points in this orthotropic plane within the admissible body are selected and highlighted following [3]. Each of these points represents a fourth-order fiber orientation tensor. For

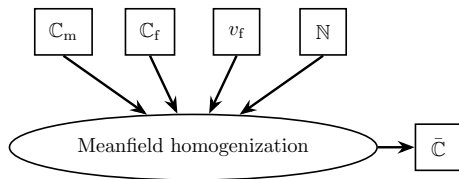


Fig. 10: Schematic representation of input and output quantities of orientation-averaging meanfield homogenization methods investigated in [3]

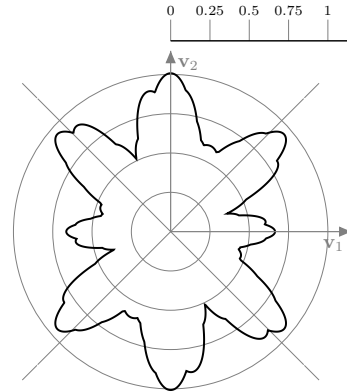


Fig. 11: Maximum relative deviation in Young's modulus $\delta(\varphi)$ in each direction among all eleven polar plots in Figure 18, i.e., selected $\mathbb{N}^{\text{planar}}(\lambda_1 = 2/3, \hat{d}_1, d_8)$ defined in overview plot Figure 15 and denoted by $\mathcal{N}^{\lambda_1=3/4}$

each point, an effective stiffness $\bar{\mathbb{C}}(\mathbb{N})$ is calculated with the Mori-Tanaka orientation averaging homogenization following Benveniste [4]. The obtained effective stiffness is partly visualized by polar plots of the direction-dependent Young's modulus $E^{\text{planar}}(\bar{\mathbb{C}}(\mathbb{N}), \varphi)$ within the plane of planarity defined by

$$E^{\text{planar}}(\mathbb{C}(\mathbb{N}), \mathbf{n}(\varphi)) = E(\mathbb{C}(\mathbb{N}), \mathbf{n}(\varphi, \theta = \pi/2)), \tag{9}$$

$$E(\mathbb{C}, \mathbf{n}(\varphi, \theta)) = \frac{\sigma(\mathbf{n}(\varphi, \theta))}{\varepsilon(\mathbf{n}(\varphi, \theta))} = [\mathbb{C}^{-1} \cdot \mathbf{n}^{\otimes 4}(\varphi, \theta)]^{-1}. \tag{10}$$

The plane of planarity is spanned by \mathbf{v}_1 and \mathbf{v}_2 and within the plane, the polar angle θ measured from the z-axis is $\theta = \pi/2$. Details on this visualization are given in [3, Equation (61) and (63)].

Similar visualizations are given for additional points within the admissible parameters space of planar fourth-order fiber orientation tensors in Figures 14 to 19. Polar plots corresponding to the points defined in the overview plot in Figure 14 are given in Figure 17. The position of the polar plots in Figure 17 mimics the position of the points within the admissible parameter space in Figure 14. The overviews in Figures 15 and 16 correspond to the polar plot views in Figures 18 and 19 respectively. The limits of all plots of the Young's modulus are equal and given by 0 GPa and 22 GPa.

6 Results and Conclusions

Thinking of fiber orientation tensors as a design space in combination with the known variety of planar fourth-order fiber orientation tensors enables a complete visualization of the directional dependence of effective Young's modulus for a given homogenization method. The proposed visualization technique can be applied to any homogenization method, see [3]. The

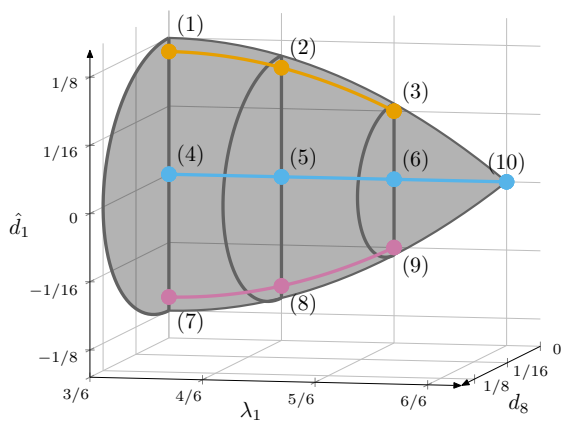


Fig. 12: Definition of ten points in the plane of planar orthotropic fiber orientation tensors of fourth-order following [3, Figure 5a]. These points are used in Figure 13

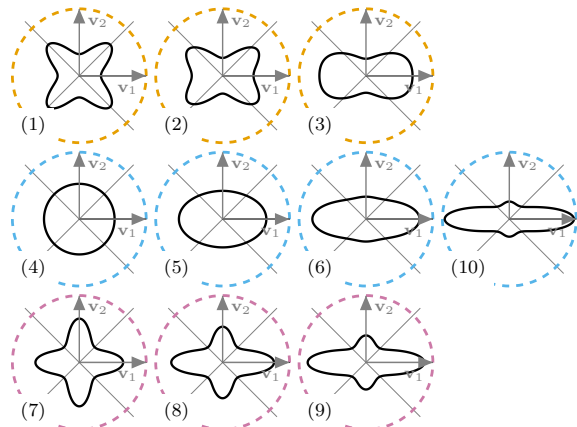


Fig. 13: Polar plots of direction-dependent Young's modulus obtained by Mori-Tanaka orientation-averaging homogenization following Benveniste [4], see [3, Figure 8a]

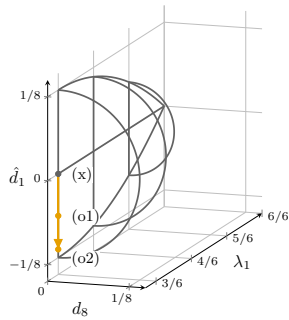


Fig. 14: Points in the plane $\lambda_1 = 1/2$ used in Figure 17 following [3, Figure 5b]

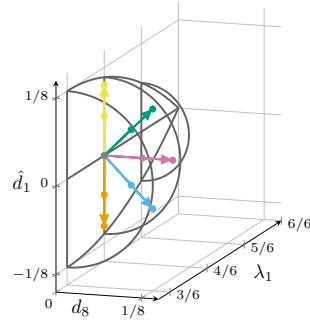


Fig. 15: Points in the plane $\lambda_1 = 2/3$ used in Figure 18 following [3, Figure 6a]

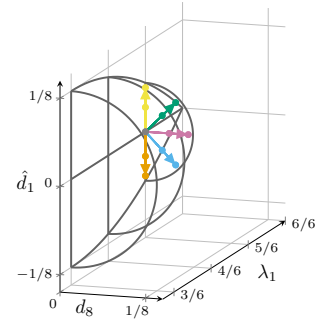


Fig. 16: Points in the plane $\lambda_1 = 5/6$ used in Figure 19 following [3, Figure 6b]

polar plots in Figure 18 are based on fiber orientation tensors with identical second-order part, as all points in the corresponding overview plot Figure 15 are placed in the plane defined by $\lambda_1 = 4/6$. In consequence, the differences in the polar plots in Figure 18 are solely based on fourth-order information within \mathbb{N} . The Young's moduli for fixed directions of different polar plots in Figure 18 differ significantly. The eleven points, i.e., fourth-order fiber orientation tensors utilized in Figure 18 are grouped to the set $\mathcal{N}^{\lambda_1=2/3}$. The maximum relative deviation of the Young's modulus among the fiber orientation tensors in $\mathcal{N}^{\lambda_1=2/3}$ is denoted by $\delta(\varphi)$ and is calculated for each direction in the plane of planarity by

$$E^{\max}(\varphi) = \max_{\mathcal{N}^{\lambda_1=2/3}} E^{\text{planar}}(\varphi, \mathbb{N}), \quad E^{\min}(\varphi) = \min_{\mathcal{N}^{\lambda_1=2/3}} E^{\text{planar}}(\varphi, \mathbb{N}), \tag{11}$$

$$\delta(\varphi) = \frac{E^{\max}(\varphi) - E^{\min}(\varphi)}{E^{\min}(\varphi)}. \tag{12}$$

The quantity $\delta(\varphi)$ is visualized as a polar plot in Figure 11. Among the inspected set of orientation tensors, the deviation $\delta(\varphi)$ varies between at least 37% and about 100%. For different sets of fiber orientation tensors this error can be significantly smaller. For the given material parameters and the selected homogenization method it is concluded that homogenization solely based on second-order fiber orientation tensor information leads to large errors in the resulting direction-dependent Young's modulus. This clearly motivates the identification and usage of fourth-order fiber orientation tensors within virtual process chains [24].

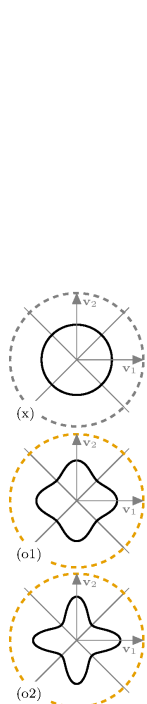


Fig. 17: Polar plots of direction-dependent Young's modulus for points defined in Figure 14, following [3, Figure 9a]

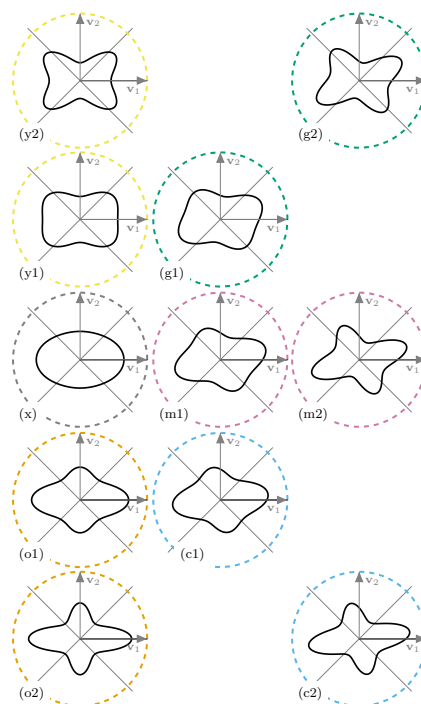


Fig. 18: Polar plots of direction-dependent Young's modulus for points defined in Figure 15, following [3, Figure 10a]

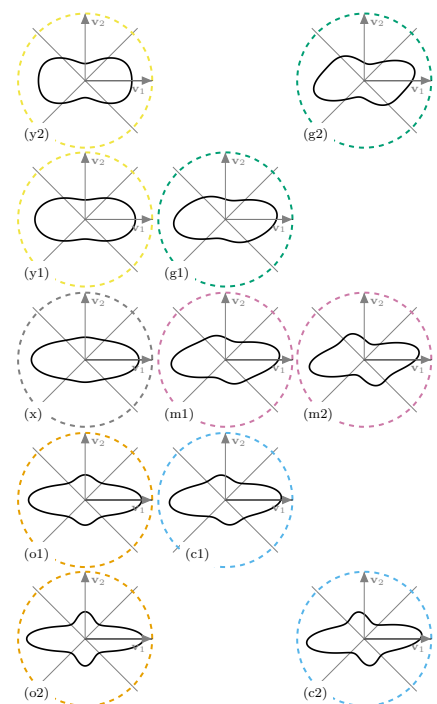


Fig. 19: Polar plots of direction-dependent Young's modulus for points defined in Figure 16, following [3, Figure 10b]

Identification of fourth-order fiber orientation tensors based on second-order directional information using closure approximations [17, 25–28] does not generate fourth-order information. For a deterministic closure approximation, closing, e.g., $\mathbb{N}^{\text{planar}}(\lambda_1 = 2/3)$ results in exactly one, hopefully admissible, $\mathbb{N}^{\text{planar}}(\lambda_1 = 2/3, d_1, d_8)$. This one-to-one mapping neglects the possible variety of $\mathbb{N}^{\text{planar}}$ of microstructures which lead to the measured or simulated $\mathbb{N}^{\text{planar}}$ and entered the closure. In addition, the intrinsic orthotropy of second-order tensors \mathbb{N} restricts outcomes of closure approximations to orthotropic \mathbb{N} . For the special case of planar fiber distributions, this implies that for any closure outcome $\mathbb{N}^{\text{planar}}(\lambda_1, d_1, d_8)$ the parameter d_8 vanishes. In consequence, the outcome of closure approximations for, e.g., $\mathbb{N}^{\text{planar}}(\lambda_1 = 2/3)$ are restricted to $\mathbb{N}^{\text{planar}}$ which lead to effective stiffnesses located between polar plots y_2, y_1, x, o_1, o_2 in Figure 18.

Acknowledgements The research documented in this presentation has been funded by the German Research Foundation (DFG, Deutsche Forschungsgemeinschaft) - project number 255730231. The support by the German Research Foundation within the International Research Training Group “Integrated engineering of continuous-discontinuous long fiber reinforced polymer structures” (GRK 2078/2) is gratefully acknowledged. Open access funding enabled and organized by Projekt DEAL.

References

- [1] J. K. Bauer and T. Böhlke, *Mathematics and Mechanics of Solids* **27**(7), 1185–1211 (2022).
- [2] J. K. Bauer and T. Böhlke, *Mathematics and Mechanics of Solids* (2022).
- [3] J. K. Bauer and T. Böhlke, *Mechanics of Materials* **170**, 104307 (2022).
- [4] Y. Benveniste, *Mechanics of Materials* **6**(2), 147 – 157 (1987).
- [5] T. Böhlke, F. Henning, A. Hrymak, L. Kärger, K. Weidenmann, and J. T. Wood, *Continuous–Discontinuous Fiber-Reinforced Polymers: An Integrated Engineering Approach* (Carl Hanser Verlag GmbH Co KG, 2019).
- [6] N. Meyer, L. Schöttl, L. Bretz, A. Hrymak, and L. Kärger, *Composites Part A: Applied Science and Manufacturing* **132**, 105809 (2020).
- [7] L. Walpole, *Journal of the Mechanics and Physics of Solids* **17**(4), 235–251 (1969).
- [8] L. Kehrer, J. T. Wood, and T. Böhlke, *Journal of Composite Materials* p. 0021998320920695 (2020).
- [9] M. Schneider, *Computational Mechanics* **59**(2), 247–263 (2017).
- [10] J. Görthofer, M. Schneider, F. Ospald, A. Hrymak, and T. Böhlke, *Computational Materials Science* **174**, 109456 (2020).
- [11] M. Schneider, *International Journal for Numerical Methods in Engineering* (2021).
- [12] A. Mehta and M. Schneider, *Computational Mechanics* pp. 1–23 (2022).
- [13] M. Schneider, *Computer Methods in Applied Mechanics and Engineering* **315**, 846–866 (2017).
- [14] D. Wicht, M. Schneider, and T. Böhlke, *International Journal for Numerical Methods in Engineering* **121**(8), 1665–1694 (2020).
- [15] A. Trauth, L. Kehrer, P. Pinter, K. Weidenmann, and T. Böhlke, *Composites Part C: Open Access* **4**, 100089 (2021).
- [16] M. Fette, *ECI Digital Archives* (2015).
- [17] J. S. Cintra Jr and C. L. Tucker III, *Journal of Rheology* **39**(6), 1095–1122 (1995).
- [18] N. Goldberg, F. Ospald, and M. Schneider, *Computational Mechanics* **60**(4), 595–611 (2017).
- [19] J. Köbler, M. Schneider, F. Ospald, H. Andrä, and R. Müller, *Computational Mechanics* **61**(6), 729–750 (2018).
- [20] W. Thomson, *Philosophical Transactions of the Royal Society of London*(146), 481–498 (1856).
- [21] J. Mandel, *International Journal of Solids and Structures* **1**(3), 273–295 (1965).
- [22] M. M. Mehrabadi and S. C. Cowin, *The Quarterly Journal of Mechanics and Applied Mathematics* **43**(1), 15–41 (1990).
- [23] J. K. Bauer, Python package “mechmean” on <https://github.com/juliankarlbauer/mechmean>, v0.1.0, 2021.
- [24] J. Görthofer, N. Meyer, T. D. Pallicity, L. Schöttl, A. Trauth, M. Schemmann, M. Hohberg, P. Pinter, P. Elsner, F. Henning, A. Hrymak, T. Seelig, K. Weidenmann, L. Kärger, and T. Böhlke, *Composites Part B: Engineering* **169**, 133–147 (2019).
- [25] S. G. Advani and C. L. Tucker III, *Journal of Rheology* **34**(3), 367–386 (1990).
- [26] K. H. Han and Y. T. Im, *Journal of Rheology* **43**(3), 569–589 (1999).
- [27] D. H. Chung and T. H. Kwon, *Journal of Rheology* **46**(1), 169–194 (2002).
- [28] S. Montgomery-Smith, W. He, D. A. Jack, and D. E. Smith, *Journal of Fluid Mechanics* **680**, 321–335 (2011).